PHYSICAL REVIEW A **95**, 043404 (2017)

Theory of time-resolved x-ray photoelectron diffraction from transient conformational molecules

Shota Tsuru,[1] Tokuei Sako,[2] Takashi Fujikawa,[1] and Akira Yagishita[3,*]
[1]*Graduate School of Advanced Integration Science, Chiba University, Yayoi-cho 1-33, Inage, Chiba 263-8522, Japan*
[2]*Laboratory of Physics, College of Science and Technology, Nihon University, 7-24-1 Narashinodai, Funabashi, Chiba 274-8501, Japan*
[3]*Photon Factory, Institute of Materials Structure Science, KEK, Oho1-1, Tsukuba, Ibaraki 305-0801, Japan*

(Received 15 December 2016; published 5 April 2017)

We formulate x-ray photoelectron diffraction (XPD) from molecules undergoing photochemical reactions induced by optical laser pulses, and then apply the formula to the simulation of time-dependent XPD profiles from both dissociating I_2 molecules and bending CS_2 molecules. The dependence of nuclear wave-packet motions on the intensity and shape of the optical laser pulses is examined. As a result, the XPD simulations based on such nuclear wave-packet calculations are observed to exhibit characteristic features, which are compared with the XPD profiles due to classical trajectories of nuclear motions. The present study provides a methodology toward creating "molecular movies" of ultrafast photochemical reactions by means of femtosecond XPD with x-ray free-electron lasers.

DOI: 10.1103/PhysRevA.95.043404

I. INTRODUCTION

The direct probing of the atomic structure of matter, static or dynamic, has always occupied an essential role in physics, chemistry, and the biological sciences [1,2]. Most of our knowledge on atomic structure has thus far been derived from x-ray and electron diffraction measurements [3–6]. However, with the advent of x-ray free-electron lasers (XFELs) [7,8], ultrafast imaging with femtosecond temporal resolution and sub-angstrom spatial resolution is becoming a very active research area with the promise of providing "molecular movies" of the dynamics of a chemical process. Indeed, apart from the more traditional approaches based on x-ray diffraction [3–5] and ultrafast electron diffraction [6,9], new methods using femtosecond pulses of the XFELs have been proposed and successfully tested on isolated free molecules. We can here refer to pump–probe gas-phase x-ray scattering [10–12] and femtosecond x-ray photoelectron diffraction [13–22]. Although the analyses of the experimental data of Refs. [11,22] heavily rely on quantum-chemical computations, there is no doubt that these experiments take a critical step toward the goal of femtosecond imaging of chemical reactions.

In this paper, we report the theoretical simulation results of time-resolved x-ray photoelectron diffraction (XPD) following the ultrafast dynamics of nuclear wave packets populated by optical laser pulses. Briefly, the present method is based on an optical laser pump–XFEL probe scheme, which is illustrated schematically in Fig. 1. An aligned or oriented molecule is first excited electronically by a short optical laser pulse, so that a nuclear wave packet on a specific potential energy surface of an electronically excited state begins to move. Its nuclear dynamics is subsequently probed by means of inner-shell XPD profiles at different time delays τ by ultrafast XFEL pulses. Theoretically, we predict the inner-shell XPD profiles as a function of the time delay τ, in which the nuclear wave-packet evolution is taken into account adiabatically. Because one of the purposes of the present work is to reveal the effects of the shape of pump-laser pulse, i.e., width and intensity, on the XPD profiles, we have performed the simulations under ideal conditions. That is, we assumed that sample molecules are fully aligned and that they are fully excited by the pump-laser pulse. Otherwise, such effects may be blurred by both insufficient alignment and mixture of excited and ground states, which depend on the experimental conditions.

The rest of the paper is organized as follows: In Sec. II, we describe the theoretical method, that is, the numerical calculations of nuclear wave packets, calculations of the XPD profile via multiple-scattering XPD (MS-XPD) theory for a fixed-nuclear geometry, and formulation of the time-resolved XPD on a path of nuclear wave-packet evolution. The main results are presented in Sec. III, where we simulate the time-dependent XPD profiles for dissociation dynamics of I_2 molecules and bending vibrational dynamics of CS_2 molecules. Finally, we summarize our study in Sec. IV.

II. THEORETICAL METHOD

A. Vibrational wave-packet motions on electronic excited-state potentials

The nonrelativistic Hamiltonian for an n-electron and N-nucleus molecule coupled with an electromagnetic field is given in atomic units as

$$H = \sum_{\alpha=1}^{N} \frac{1}{2M_\alpha}[\boldsymbol{P}_\alpha - Z_\alpha \boldsymbol{A}(\boldsymbol{R}_\alpha,t)]^2 + \sum_{i=1}^{n} \frac{1}{2}[\boldsymbol{p}_i + \boldsymbol{A}(\boldsymbol{r}_i,t)]^2 - \sum_{i=1}^{n}\sum_{\alpha=1}^{N} \frac{Z_\alpha}{|\boldsymbol{R}_\alpha - \boldsymbol{r}_i|} + \sum_{\alpha>\beta}^{N} \frac{Z_\alpha Z_\beta}{|\boldsymbol{R}_\alpha - \boldsymbol{R}_\beta|} + \sum_{i>j}^{n} \frac{1}{|\boldsymbol{r}_i - \boldsymbol{r}_j|}, \tag{1}$$

where $\{\boldsymbol{r}_i\}$, $\{\boldsymbol{R}_\alpha\}$, $\{Z_\alpha\}$, $\boldsymbol{A}(\boldsymbol{r}_i,t)$, and $\boldsymbol{A}(\boldsymbol{R}_\alpha,t)$ represent the spatial coordinates of the ith electron, that of the αth nucleus, the charge of the αth nucleus, and the time-dependent vector potentials of electromagnetic fields at the positions of the ith electron and at the αth nucleus, respectively. Next, with the use of the abbreviations of $\boldsymbol{R} = \{\boldsymbol{R}_1, \boldsymbol{R}_2, \ldots, \boldsymbol{R}_N\}$ and $\boldsymbol{r} = \{\boldsymbol{r}_1, \boldsymbol{r}_2, \ldots, \boldsymbol{r}_n\}$, the time-dependent Schrödinger equation

---

[*] akira.yagishita@kek.jp

2469-9926/2017/95(4)/043404(9)

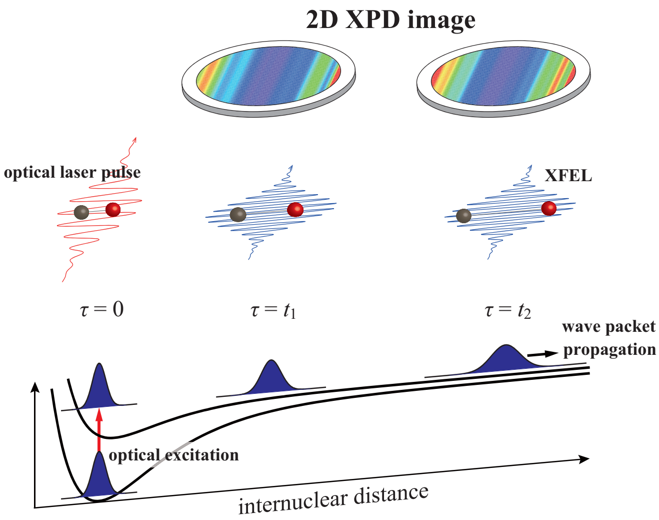

FIG. 1. Sketch of an optical laser pump–XFEL probe experimental scheme. An optical laser prepares vibrational wave packets on an excited state. They are then probed by means of XPD images with XFEL pulses.

(TDSE) for this system is written as

$$i\frac{\partial}{\partial t}\Psi(\boldsymbol{R},\boldsymbol{r},t) = H\Psi(\boldsymbol{R},\boldsymbol{r},t). \tag{2}$$

By implementation of the dipole approximation of $\boldsymbol{A}(\boldsymbol{R}_\alpha,t) \cong \boldsymbol{A}(t)$ and $\boldsymbol{A}(\boldsymbol{r}_i,t) \cong \boldsymbol{A}(t)$ and the unitary transformation of $\Pi_{\alpha=1}^{N}\exp[-iZ_\alpha\boldsymbol{A}(t)\cdot\boldsymbol{R}_\alpha]\Pi_{i=1}^{n}\exp[-i\boldsymbol{A}(t)\cdot\boldsymbol{r}_i]$ to the wave function $\Psi(\boldsymbol{R},\boldsymbol{r},t)$ in Eq. (2), the TDSE is expressed as

$$\begin{aligned} i\frac{\partial}{\partial t}\Psi(\boldsymbol{R},\boldsymbol{r},t) = \Bigg[&\sum_{\alpha=1}^{N}\frac{\boldsymbol{P}_\alpha{}^2}{2M_\alpha} + \sum_{i=1}^{n}\frac{\boldsymbol{p}_i{}^2}{2} + \boldsymbol{E}(t)\cdot\sum_{i=1}^{n}\boldsymbol{r}_i \\ &- \sum_{i=1}^{n}\sum_{\alpha=1}^{N}\frac{Z_\alpha}{|\boldsymbol{R}_\alpha - \boldsymbol{r}_i|} + \sum_{\alpha>\beta}^{N}\frac{Z_\alpha Z_\beta}{|\boldsymbol{R}_\alpha - \boldsymbol{R}_\beta|} \\ &+ \sum_{i>j}^{n}\frac{1}{|\boldsymbol{r}_i - \boldsymbol{r}_j|}\Bigg]\Psi(\boldsymbol{R},\boldsymbol{r},t), \end{aligned} \tag{3}$$

where $\boldsymbol{E}(t) = -\partial\boldsymbol{A}(t)/\partial t$. In Eq. (3), the interaction between the nucleus and the electromagnetic field is neglected.

Here, we introduce the Hamiltonian for electrons without external fields at the fixed nuclear position of $\boldsymbol{R}$:

$$H_{el}(\boldsymbol{R}) = \sum_{i=1}^{n}\frac{\boldsymbol{p}_i{}^2}{2} - \sum_{i=1}^{n}\sum_{\alpha=1}^{N}\frac{Z_\alpha}{|\boldsymbol{R}_\alpha - \boldsymbol{r}_i|} + \sum_{i>j}^{n}\frac{1}{|\boldsymbol{r}_i - \boldsymbol{r}_j|}. \tag{4}$$

Next, under the two-level approximation we consider the ground- and excited-state electronic wave functions of $\Phi_g(\boldsymbol{r};\boldsymbol{R})$ and $\Phi_e(\boldsymbol{r};\boldsymbol{R})$, which satisfy the following time-independent Schrödinger equations:

$$\begin{aligned} H_{el}(\boldsymbol{R})\Phi_g(\boldsymbol{r};\boldsymbol{R}) &= \varepsilon_g(\boldsymbol{R})\Phi_g(\boldsymbol{r};\boldsymbol{R}), \\ H_{el}(\boldsymbol{R})\Phi_e(\boldsymbol{r};\boldsymbol{R}) &= \varepsilon_e(\boldsymbol{R})\Phi_e(\boldsymbol{r};\boldsymbol{R}). \end{aligned} \tag{5}$$

In this context, the wave function $\Psi(\boldsymbol{R},\boldsymbol{r},t)$, which satisfies the TDSE of Eq. (3), can be expressed by the superposition of $\Phi_g(\boldsymbol{r};\boldsymbol{R})$ and $\Phi_e(\boldsymbol{r};\boldsymbol{R})$ as follows:

$$\Psi(\boldsymbol{R},\boldsymbol{r},t) = \chi_g(\boldsymbol{R},t)\Phi_g(\boldsymbol{r};\boldsymbol{R}) + \chi_e(\boldsymbol{R},t)\Phi_e(\boldsymbol{r};\boldsymbol{R}). \tag{6}$$

By inserting Eq. (6) into Eq. (3), we derive the following coupled TDSE for the nuclear wave packets:

$$\begin{aligned} &i\frac{\partial}{\partial t}\begin{pmatrix}\chi_g(\boldsymbol{R},t)\\ \chi_e(\boldsymbol{R},t)\end{pmatrix} \\ &= \begin{pmatrix} \sum_{\alpha=1}^{N}\frac{\boldsymbol{P}_\alpha{}^2}{2M_\alpha} + V_g(\boldsymbol{R}) & \boldsymbol{E}(t)\cdot\langle\Phi_g|\sum_{i=1}^{n}\boldsymbol{r}_i|\Phi_e\rangle \\ \boldsymbol{E}(t)\cdot\langle\Phi_e|\sum_{i=1}^{n}\boldsymbol{r}_i|\Phi_g\rangle & \sum_{\alpha=1}^{N}\frac{\boldsymbol{P}_\alpha{}^2}{2M_\alpha} + V_e(\boldsymbol{R}) \end{pmatrix} \\ &\quad\times\begin{pmatrix}\chi_g(\boldsymbol{R},t)\\ \chi_e(\boldsymbol{R},t)\end{pmatrix}, \end{aligned} \tag{7}$$

where $V_{g(e)}(\boldsymbol{R})$ denotes the potential of the nuclei, i.e.,

$$V_{g(e)}(\boldsymbol{R}) = \varepsilon_{g(e)}(\boldsymbol{R}) + \sum_{\alpha>\beta}^{N}\frac{Z_\alpha Z_\beta}{|\boldsymbol{R}_\alpha - \boldsymbol{R}_\beta|}. \tag{8}$$

In Eq. (7), the vibronic interaction is neglected, which may be valid within the framework of the Born-Oppenheimer approximation.

The TDSE of Eq. (7) for the vibrational wave packets can be integrated for an infinitesimal time step Δt by a standard computational technique, such as a split-operator method [23] or a higher-order symplectic integrator method [24]:

$$\begin{aligned} \begin{pmatrix}\chi_g(\boldsymbol{R},t+\Delta t)\\ \chi_e(\boldsymbol{R},t+\Delta t)\end{pmatrix} &\approx \exp(-i\Delta tT/2)\exp[-i\Delta tV(t)] \\ &\quad\times\exp(-i\Delta tT/2)\begin{pmatrix}\chi_g(\boldsymbol{R},t)\\ \chi_e(\boldsymbol{R},t)\end{pmatrix}, \end{aligned} \tag{9}$$

where

$$T \equiv \begin{pmatrix} \sum_{\alpha=1}^{N}\frac{\boldsymbol{P}_\alpha{}^2}{2M_\alpha} & 0 \\ 0 & \sum_{\alpha=1}^{N}\frac{\boldsymbol{P}_\alpha{}^2}{2M_\alpha} \end{pmatrix} \tag{10}$$

and

$$V(t) \equiv \begin{pmatrix} V_g(\boldsymbol{R}) & \boldsymbol{E}(t)\cdot\langle\Phi_g|\sum_{i=1}^{n}\boldsymbol{r}_i|\Phi_e\rangle \\ \boldsymbol{E}(t)\cdot\langle\Phi_e|\sum_{i=1}^{n}\boldsymbol{r}_i|\Phi_g\rangle & V_e(\boldsymbol{R}) \end{pmatrix}. \tag{11}$$

The initial condition for the iteration of Eq. (9) is given by

$$\chi_g(\boldsymbol{R},t=-\infty) = \chi_g(\boldsymbol{R}) \quad \text{and} \quad \chi_e(\boldsymbol{R},t=-\infty) = 0. \tag{12}$$

Namely, the iteration begins from the ground-state vibrational wave function $\chi_g(\boldsymbol{R})$. Since the norm of $\chi_g(\boldsymbol{R})$ is normalized to unity, the integral of $|\chi_{g(e)}(\boldsymbol{R},t)|^2$ over the nuclear coordinate $\boldsymbol{R}$ yields the population of the electronic ground (excited) state. In practical nuclear wave-packet calculations, the normal coordinates are used instead of the spatial coordinates.

In this study, we assumed a Gaussian-shaped pulse for optical lasers:

$$\boldsymbol{E}(t) = \boldsymbol{E}_0 \exp[-\ln 2(2t/\Gamma)^2] \cos \omega_0 t, \qquad (13)$$

where $\boldsymbol{E}_0$, ω_0, and Γ represent the electric field strength, central frequency, and temporal pulse width of the laser, respectively. The atomic unit of the electric field strength is the field experienced by an electron in the ground state of atomic hydrogen, $E_0 = 5.14 \times 10^9$ V/cm, and the corresponding laser intensity is $I_0 = 3.51 \times 10^{16}$ W/cm^2.

B. Multiple-scattering x-ray photoelectron diffraction

Under the sudden approximation, the amplitude of core-level photoemission from an electronically excited molecule is expressed as [14]

$$\begin{aligned} &\langle \psi_{\boldsymbol{k}}^-(\boldsymbol{r};\boldsymbol{R})\Phi_h(\boldsymbol{r}^{n-1};\boldsymbol{R})|\hat{\boldsymbol{e}}\cdot\boldsymbol{r}|\Phi_e(\boldsymbol{r};\boldsymbol{R})\rangle \\ &\quad \approx \langle \psi_{\boldsymbol{k}}^-(\boldsymbol{r}_A;\boldsymbol{R})|\hat{\boldsymbol{e}}\cdot\boldsymbol{r}_A|\phi_c(\boldsymbol{r}_A)\rangle, \qquad (14) \end{aligned}$$

where $\psi_{\boldsymbol{k}}^-(\boldsymbol{r}_A;\boldsymbol{R})$ represents the photoelectron wave function of momentum $\boldsymbol{k}$ under the influence of the optical potential, $\phi_c(\boldsymbol{r}_A)$ is the wave function of a core orbital localized on the atomic site A, and $\hat{\boldsymbol{e}}$ is the polarization vector of XFEL. The atomic wave function $\phi_c(\boldsymbol{r}_A)$ may hardly be influenced by the molecular structure, whereas one can consider that the photoelectron wave function $\psi_{\boldsymbol{k}}^-(\boldsymbol{r}_A;\boldsymbol{R})$ depends on a transient molecular structure. Assuming these simple descriptions for the wave functions, the one-electron matrix element of Eq. (14) is calculated relying on the MS-XPD theory [14,25–27].

By use of the site-t matrix expansion of $\psi_{\boldsymbol{k}}^-(\boldsymbol{r}_A;\boldsymbol{R})$ [25], the photoemission amplitude can be expressed as the multiple-scattering series

$$\langle \psi_{\boldsymbol{k}}^-(\boldsymbol{r}_A;\boldsymbol{R})|\hat{\boldsymbol{e}}\cdot\boldsymbol{r}_A|\phi_c(\boldsymbol{r}_A)\rangle = Z_0 + Z_1 + Z_2 + \cdots, \qquad (15)$$

where Z_0 represents the amplitude without scattering from surrounding atoms (direct term), Z_1 is the single-scattering amplitude, Z_2 is the double-scattering amplitude, and so on. The direct term Z_0 is written as

$$Z_0 = \langle \phi_{A\boldsymbol{k}}^- |\hat{\boldsymbol{e}}\cdot\boldsymbol{r}_A|\phi_c\rangle = \sum_{lm} Y_{lm}(\hat{\boldsymbol{k}}) M_{lm,l_c m_c}, \qquad (16)$$

where $\phi_{A\boldsymbol{k}}^-$ denotes the wave function for the photoelectron with momentum $\boldsymbol{k}$ emitted from an atom A absorbing an x-ray, and l and m are the azimuthal and magnetic quantum numbers, respectively. In the dipole approximation, the photoionization matrix element $M_{lm,l_c m_c}$ excited by linearly polarized x-rays parallel to the z axis is given by

$$\begin{aligned} M_{lm,\,l_c m_c} = &\sqrt{\frac{2}{\pi}} i^{-l} e^{i\delta_l^A} \int {r_A}^2 dr_A R_{\varepsilon l}(r_A) r_A R_{nl_c}(r_A) \\ &\times \int d\hat{\boldsymbol{r}}_A Y_{lm}^*(\hat{\boldsymbol{r}}_A) \sqrt{\frac{4\pi}{3}} Y_{10}(\hat{\boldsymbol{r}}_A) Y_{l_c m_c}(\hat{\boldsymbol{r}}_A), \qquad (17) \end{aligned}$$

where δ_l^A represents the phase shift of the lth partial wave at site A, and $R_{\varepsilon l}(r_A)$ and $R_{nl_c}(r_A)$ are the radial part labeled by the angular momentum quantum numbers (l,m) and (l_c,m_c) for $\phi_{A\boldsymbol{k}}^-$ and ϕ_c, respectively. The integral for the angular part yields the angular momentum selection rule of the photoionization.

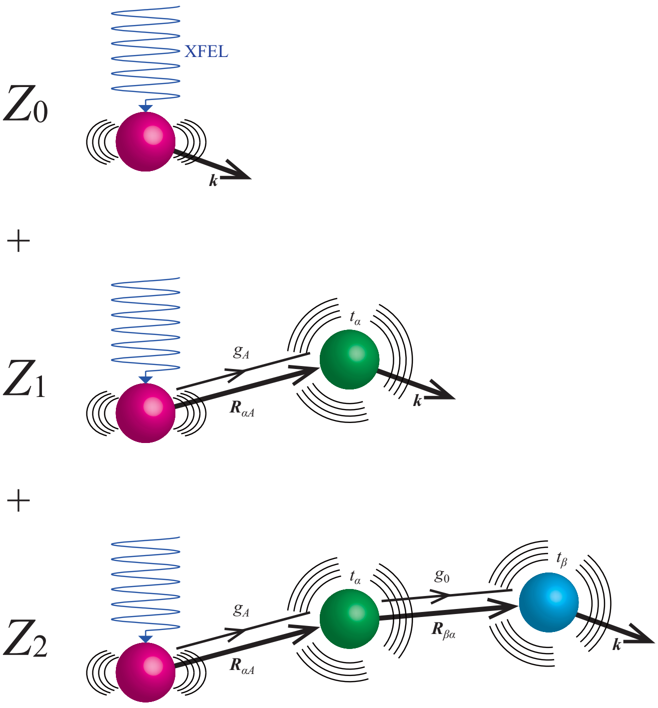

FIG. 2. Pictorial representations of the multiple-scattering series of Z_0, Z_1, and Z_2. See text for abbreviations.

The single-scattering term Z_1 is explicitly written as

$$\begin{aligned} Z_1 &= \sum_{\alpha(\neq A)} \langle \phi_{\boldsymbol{k}}^0 | t_\alpha g_A \hat{\boldsymbol{e}}\cdot\boldsymbol{r}_A|\phi_c\rangle \\ &= \sum_{\alpha(\neq A)} e^{-i\boldsymbol{k}\cdot\boldsymbol{R}_{\alpha A}} \sum_{lm,\,l'm'} Y_{l'm'}(\hat{\boldsymbol{k}}) t_{l'}^\alpha(k) G_{l'm',\,lm}(k\boldsymbol{R}_{\alpha A}) M_{lm,\,l_c m_c}, \end{aligned} \qquad (18)$$

where $\phi_{\boldsymbol{k}}^0$ denotes the plane wave and $\boldsymbol{R}_{\alpha A}$ is the position vector of scatterer α measured from the photoelectron emitter A. g_A is expressed by the Green function g_0 and site-t matrix t_A: $g_A = g_0 + g_0 t_A g_0$ (see Fig. 2) [26,27]. The angular momentum representation of site-t matrix t_l^α at site α is given due to the phase shift $\delta_l^\alpha(k)$ as

$$t_l^\alpha(k) = -\frac{\exp\left[2i\delta_l^\alpha(k)\right] - 1}{2ik}. \qquad (19)$$

The propagator $G_{l'm',\,lm}(k\boldsymbol{R}_{\alpha A})$ describes electron propagation from site A with (l,m) to site α with (l',m') [14,25]. By introducing $X = tG$, we can obtain the general renormalized multiple-scattering XPD formula [14,25–27] as

$$\begin{aligned} &\langle \psi_{\boldsymbol{k}}^-(\boldsymbol{r}_A;\boldsymbol{R})|\hat{\boldsymbol{e}}\cdot\boldsymbol{r}_A|\phi_c(\boldsymbol{r}_A)\rangle \\ &\quad = \sum_\alpha e^{-i\boldsymbol{k}\cdot\boldsymbol{R}_{\alpha A}} \sum_{lm,\,l'm'} Y_{l'm'}(\hat{\boldsymbol{k}}) \{1 + X + X^2 \\ &\qquad + X^3 + \cdots\}_{l'm',\,lm}^{\alpha A} M_{lm,\,l_c m_c}, \\ &\quad = \sum_\alpha e^{-i\boldsymbol{k}\cdot\boldsymbol{R}_{\alpha A}} \sum_{lm,\,l'm'} Y_{l'm'}(\hat{\boldsymbol{k}}) \{[1 - X]^{-1}\}_{l'm',\,lm}^{\alpha A} M_{lm,\,l_c m_c} \end{aligned} \qquad (20)$$

$$X_{lm,\,l'm'}^{\alpha\beta} = (1 - \delta^{\alpha\beta}) t_l^\alpha(k) G_{lm,\,l'm'}(k\boldsymbol{R}_{\alpha\beta}), \qquad (21)$$

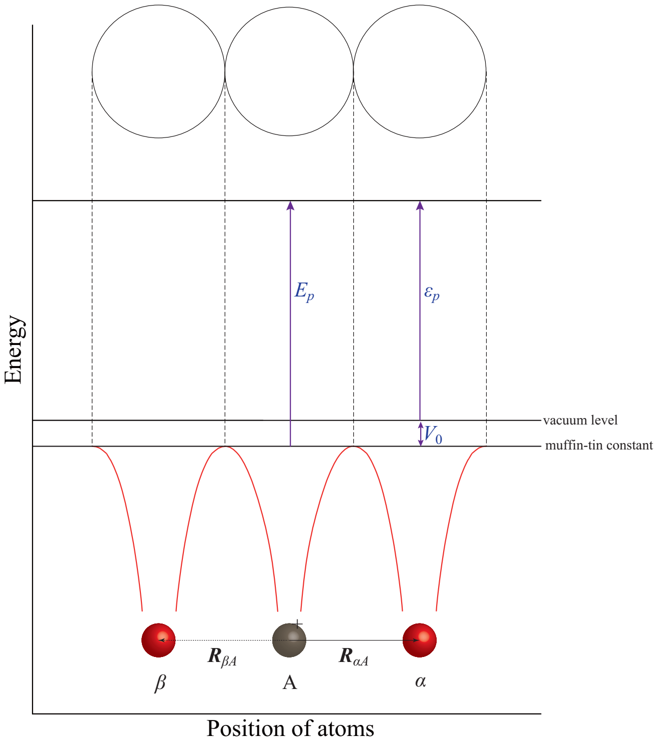

FIG. 3. Muffin-tin potential of a triatomic molecule. ε_p: photoelectron kinetic energy from the vacuum level, V_0: energy between the vacuum level and the muffin-tin constant, and E_p: photoelectron energy in the molecular region.

where X denotes a square matrix in which a matrix element is labeled by a set of atomic sites $(A, \alpha, \beta, \dots)$ in a molecule and the pair of angular momentum numbers (l,m). The dimension of the matrix is $N(l_{\max}+1)^2$ for a molecule having N atoms and maximum angular momentum $l_{\max}$. The full multiple scattering is taken into account by use of the inverse matrix $(1-X)^{-1}$. Thus we can obtain an XPD profile $d\sigma/d\hat{\boldsymbol{k}}(\boldsymbol{R})$ by carrying out the calculations of the MS-XPD formula:

$$\frac{d\sigma}{d\hat{\boldsymbol{k}}}(\boldsymbol{R}) \propto |\langle \psi_{\boldsymbol{k}}^{-}(\boldsymbol{r}_A;\boldsymbol{R})|\hat{\boldsymbol{e}}\cdot\boldsymbol{r}_A|\phi_c(\boldsymbol{r}_A)\rangle|^2. \tag{22}$$

As can be understood from the above discussion, the XPD profile contains information on the molecular structure through the position vectors of $\boldsymbol{R}_{\alpha\beta}$ in the MS-XPD calculations. That is to say, in this work, such a molecular structure, which is defined by a set of positions for atomic sites $(A, \alpha, \beta, \dots)$, is described by a muffin-tin potential. A schematic of the one-dimensional (1D) muffin-tin potential for a triatomic molecule is shown in Fig. 3. The muffin-tin constant is generally different from the vacuum level. Therefore, the photoelectron energy experienced in the molecular region E_p is described by $E_p = \varepsilon_p + V_0$, where ε_p denotes the photoelectron kinetic energy measured from the vacuum level and V_0 the energy between the vacuum level and the muffin-tin constant. We evaluated the muffin-tin radii and muffin-tin zero energy of V_0 from each of the atomic potentials $-Z/r + V_{\mathrm{HF}}$, where the center-of-gravity energy of V_{HF} was calculated using the Hartree-Fock program of Cowan [28]. Namely, we prepared atomic potentials centered on the emitter atom and the neighboring atoms to determine the muffin-tin radii and V_0. It should be noted that for the photoelectron kinetic energy >100 eV experimental XPD profiles of various molecules were well reproduced by the MS-XPD calculations employing the muffin-tin potentials (Refs. [14,27] and references therein).

C. Time-resolved x-ray photoelectron diffraction from photoexcited molecules

Theoretically, a time-resolved XPD profile $d\sigma/d\hat{\boldsymbol{k}}(\boldsymbol{R},\tau)$ with ultrafast XFEL pulses at a time delay τ after a pump pulse can be formulated as

$$\frac{d\sigma}{d\hat{\boldsymbol{k}}}(\boldsymbol{R},\tau) \propto \int d\boldsymbol{R}|\chi_e(\boldsymbol{R},\tau)|^2|\langle \psi_{\boldsymbol{k}}^{-}(\boldsymbol{r}_A;\boldsymbol{R})|\hat{\boldsymbol{e}}\cdot\boldsymbol{r}_A|\phi_c(\boldsymbol{r}_A)\rangle|^2. \tag{23}$$

Here, $\chi_e(\boldsymbol{R},\tau)$ represents the nuclear wave packet induced by the optical laser pulses and $|\langle \psi_{\boldsymbol{k}}^{-}(\boldsymbol{r}_A;\boldsymbol{R})|\hat{\boldsymbol{e}}\cdot\boldsymbol{r}_A|\phi_c(\boldsymbol{r}_A)\rangle|^2$ is the XPD profile for the molecular structure described by the set of position vectors $\boldsymbol{R}$. The above equation can be derived within the Chase adiabatic approximation [29] under the assumption that nuclei are frozen during the probe pulse. For the applications of Eq. (23), we used the $\chi_e(\boldsymbol{R},\tau)$, which was obtained by solving Eq. (7) numerically for typical intensities and pulse widths of available optical lasers. Next, we used the $\boldsymbol{R}$-dependent XPD profiles, which were calculated with use of Eq. (22) assuming the muffin-tin potentials. It should be noted that we assumed that the phase shift $\delta_l^{\alpha}(k)$ was constant over $\boldsymbol{R}$.

A few remarks on our simulations are in order. The duration of the ultrafast XFEL pulses is not taken into account, and convolution of XPD profiles $d\sigma/d\hat{\boldsymbol{k}}(\boldsymbol{R})$ over the photon spectral bandwidth is not carried out. These two points must be taken into account when we analyze time-dependent XPD data.

III. RESULTS

A. I_2 molecules

We consider time-resolved XPD imaging for the photoexcited dissociation process of I_2 molecules with the ultrafast XFEL pulses: Aligned I_2 molecules are first excited

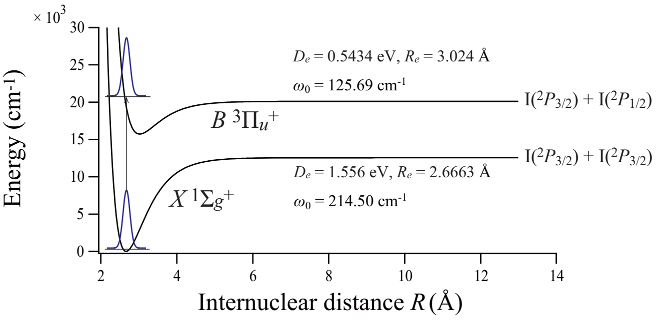

FIG. 4. Potential energy curves of an I_2 molecule. A vibrational wave packet is induced on the $B\ ^3\Pi_u{}^+$ state.

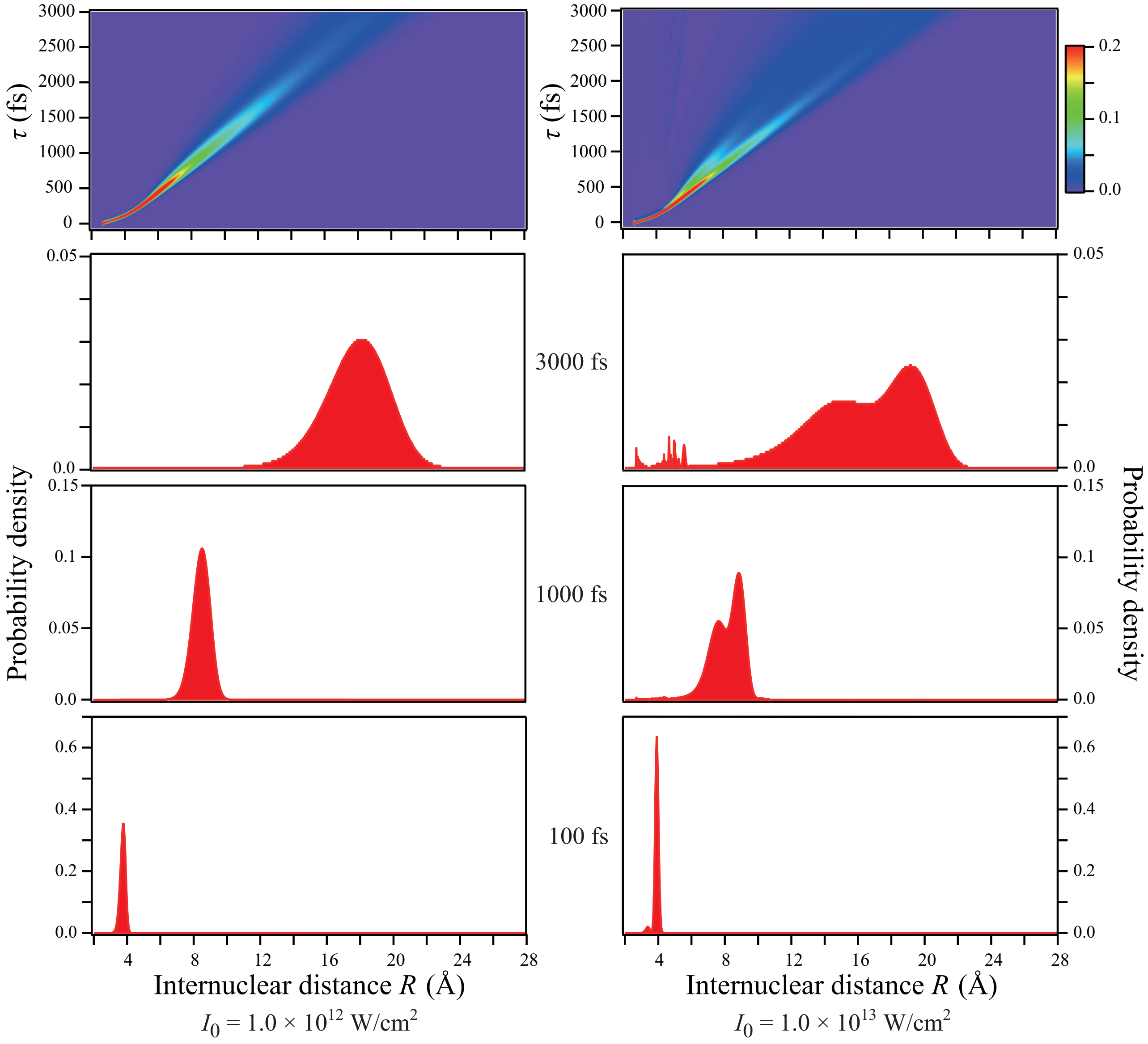

FIG. 5. Nuclear wave-packet evolutions on the state $B\,{}^3\Pi_u{}^+$ state of the I_2 molecule. Left column: laser intensity of $I_0 = 1.0\times10^{12}\,\mathrm{W/cm^2}$ with pulse width of $\Gamma = 50\,\mathrm{fs}$. Right column: laser intensity of $I_0 = 1.0\times10^{13}\,\mathrm{W/cm^2}$ with pulse width of $\Gamma = 50\,\mathrm{fs}$. Upper panels: the wave-packet evolutions expressed as functions of the delay time τ and internuclear distance R. Lower panels: cross sections at $\tau = 100$, 1000, and 3000 fs of the upper panels. Vertical scales of $|\chi_e(\boldsymbol{R},t)|^2$ are normalized intensities; the norm of $\chi_g(\boldsymbol{R})$ is normalized to unity, so that the integral of $|\chi_e(\boldsymbol{R},t)|^2$ over the stretching nuclear coordinate $\boldsymbol{R}$ yields the population of the electronic excited state; 26.5% for $I_0 = 1.0\times10^{12}\,\mathrm{W/cm^2}$ and $\Gamma = 50$ fs, 31.7% for $I_0 = 1.0\times10^{13}\,\mathrm{W/cm^2}$ and $\Gamma = 50\,\mathrm{fs}$.

electronically to the $B\,{}^3\Pi_u{}^+$ state by optical laser pulses with centered wavelength $\lambda_0 = 485\,\mathrm{nm}\,(206\times10^2\,\mathrm{cm^{-1}})$ and temporal width $\Gamma = 50\,\mathrm{fs}$ [30]. Due to this pump laser, nuclear wave packets created on the specific potential energy surface start to move. Their nuclear dynamics is later probed at a different time delay by means of I 3s XPD profiles of I_2 molecules with XFEL pulses. In this pump–probe scheme, the polarization vectors of the two lasers are parallel to the molecular axis of the aligned I_2 molecules.

In calculating the vibrational wave packets on the $B\,{}^3\Pi_u{}^+$ state, we used the spectroscopic constants of the dissociation energy, equilibrium internuclear distance, and fundamental frequency given in Refs. [31,32], and the analytical forms of transition moments in Ref. [33]. The relevant potential energy curves are shown in Fig. 4. To examine the laser intensity I_0 dependence of vibrational wave-packet evolution, we calculated the vibrational wave packets for both $I_0 = 1.0\times10^{12}\,\mathrm{W/cm^2}$ and $I_0 = 1.0\times10^{13}\,\mathrm{W/cm^2}$. Figure 5 shows the simulation results of the vibrational wave-packet evolution. For $I_0 = 1.0\times10^{12}\,\mathrm{W/cm^2}$, the nuclear wave packets simply spread and move on the potential curve. In contrast, for $I_0 = 1.0\times10^{13}\,\mathrm{W/cm^2}$, the nuclear wave packet splits into two peaks. This interesting phenomenon may be due to Rabi oscillations for

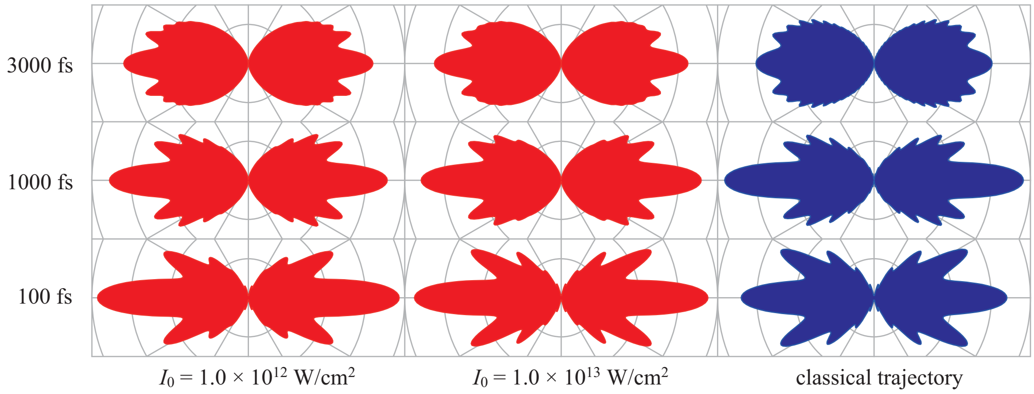

FIG. 6. Time-resolved I 3s XPD profiles of I_2 molecules. The delay times are written on the left of the panel. Left: laser intensity of $I_0 = 1.0\times10^{12}\,\mathrm{W/cm^2}$ with pulse width of $\Gamma = 50\,\mathrm{fs}$, middle: laser intensity of $I_0 = 1.0\times10^{13}\,\mathrm{W/cm^2}$ with pulse width of $\Gamma = 50\,\mathrm{fs}$, and right: a classical trajectory.

two-level systems with radiation fields satisfying resonant conditions [34].

In our calculations of the XPD profile $d\sigma/d\hat{\boldsymbol{k}}(\boldsymbol{R})$, we selected an XFEL photon energy of 1222 eV, which is 150 eV above the I 3s ionization threshold of 1072 eV [35]. Photoemissions from the gerade and ungerade molecular orbitals of the I_2 molecules cannot be resolved with the broad bandpass of XFEL, so that the XPD profile was calculated as the incoherent sum of those from the left and right I atoms in I_2 molecules. Next, using the vibrational wave-packet evolution results on the $B\,{}^3\Pi_u{}^+$ state and the XPD profile $d\sigma/d\hat{\boldsymbol{k}}(\boldsymbol{R})$, we simulated the time-resolved I 3s XPD profiles of I_2 molecules probed by the ultrafast XFEL pulses as a function of the pump–probe delay time τ. The time-resolved I 3s XPD profiles, induced by the pump laser with $I_0 = 1.0\times10^{12}\,\mathrm{W/cm^2}$ and $I_0 = 1.0\times10^{13}\,\mathrm{W/cm^2}$, are shown in Fig. 6. For comparison, the XPD profiles for a classical trajectory of the nuclear motions are also shown. Integrated areas of the XPD profiles are normalized to unity. As can be observed from the figure, the time-resolved XPD profiles on a path of the nuclear wave-packet evolution and that for the classical trajectory are similar to each other overall. However, we can observe that the fine structures of the XPD profiles for the classical trajectory are blurred in those based on the wave-packet calculations due to the conspicuous spreads of the nuclear wave packets at $\tau = 1000$ and 3000 fs, particularly for $I_0 = 1.0\times10^{13}\,\mathrm{W/cm^2}$ (see Fig. 5).

B. CS_2 molecules

In this section, we discuss the time-resolved XPD imaging of photochemical reactions of CS_2 molecules. Photoexcitation from ${}^1\Sigma_g{}^+$ to ${}^1B_2\,({}^1\Sigma_u{}^+)$ in the wavelength region of 192–208 nm ($43000{-}54000\,\mathrm{cm^{-1}}$) makes the molecule a bent (or quasilinear) structure and includes symmetric stretching ($\nu_1 = 392\,\mathrm{cm^{-1}}$) and bending ($\nu_2 = 426\,\mathrm{cm^{-1}}$) vibrations [36,37]. At a centered wavelength of $\lambda_0 = 198\,\mathrm{nm}$ ($505\times10^2\,\mathrm{cm^{-1}}$), the molecule is above the barrier for linearity, so that a large bending vibration occurs between the linear and bent geometries. The nuclear dynamics is probed by means of time-resolved C 1s XPD profiles of CS_2 molecules with ultrafast XFEL pulses at different time delays. The polarization vector of the pump laser is perpendicular to the S–S direction of CS_2 molecules and that of the probe laser is parallel to the direction in the simulations. We used the potential energy curve of a 1D quadrupole curve along the S–C–S bond angle, which was derived by Douglas and Zanon [36] and Arendt and Butler [38]. Such a potential curve is plotted in Fig. 7. Further, we used the dipole moment for the ${}^1\Sigma_g{}^+ \rightarrow {}^1B_2\,({}^1\Sigma_u{}^+)$ transition, i.e., the oscillator strength ($f = 1.024$) in Ref. [39]. The oscillator strength is weighted by the nuclear wave function of the ${}^1\Sigma_g{}^+$ state and the nuclear wave packet of the ${}^1B_2\,({}^1\Sigma_u{}^+)$ state, then averaged over all the geometries in the Franck-Condon region. To investigate the pulse-width dependence on vibrational wave-packet evolution, we calculated the vibrational wave packets for $\Gamma = 7$ and 20 fs at the laser intensity of $I_0 = 3.0\times10^{11}\,\mathrm{W/cm^2}$. Figure 8 shows the simulation results. The nuclear wave packets exhibit oscillatory motions for both cases: for $\Gamma = 7\,\mathrm{fs}$ the linear structure at $\tau = 80\,\mathrm{fs}$ revives at $\tau = 160\,\mathrm{fs}$, and for $\Gamma = 20\,\mathrm{fs}$ the linear structure at $\tau = 50\,\mathrm{fs}$ revives at $\tau =$

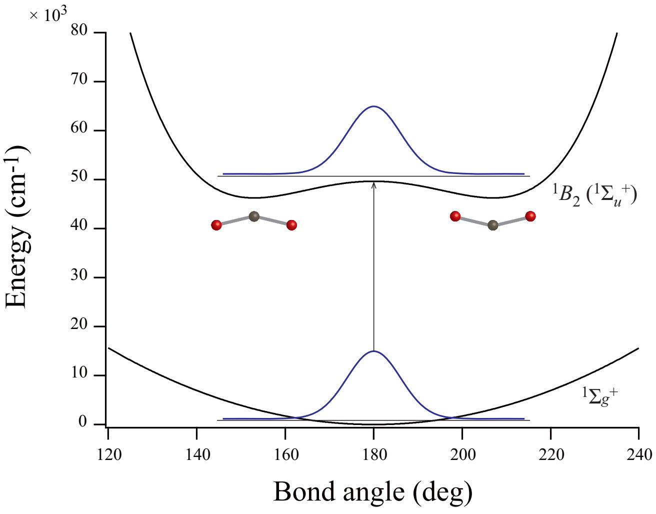

FIG. 7. Potential energy curves of a CS_2 molecule. A vibrational wave packet is induced on the ${}^1B_2$ state.

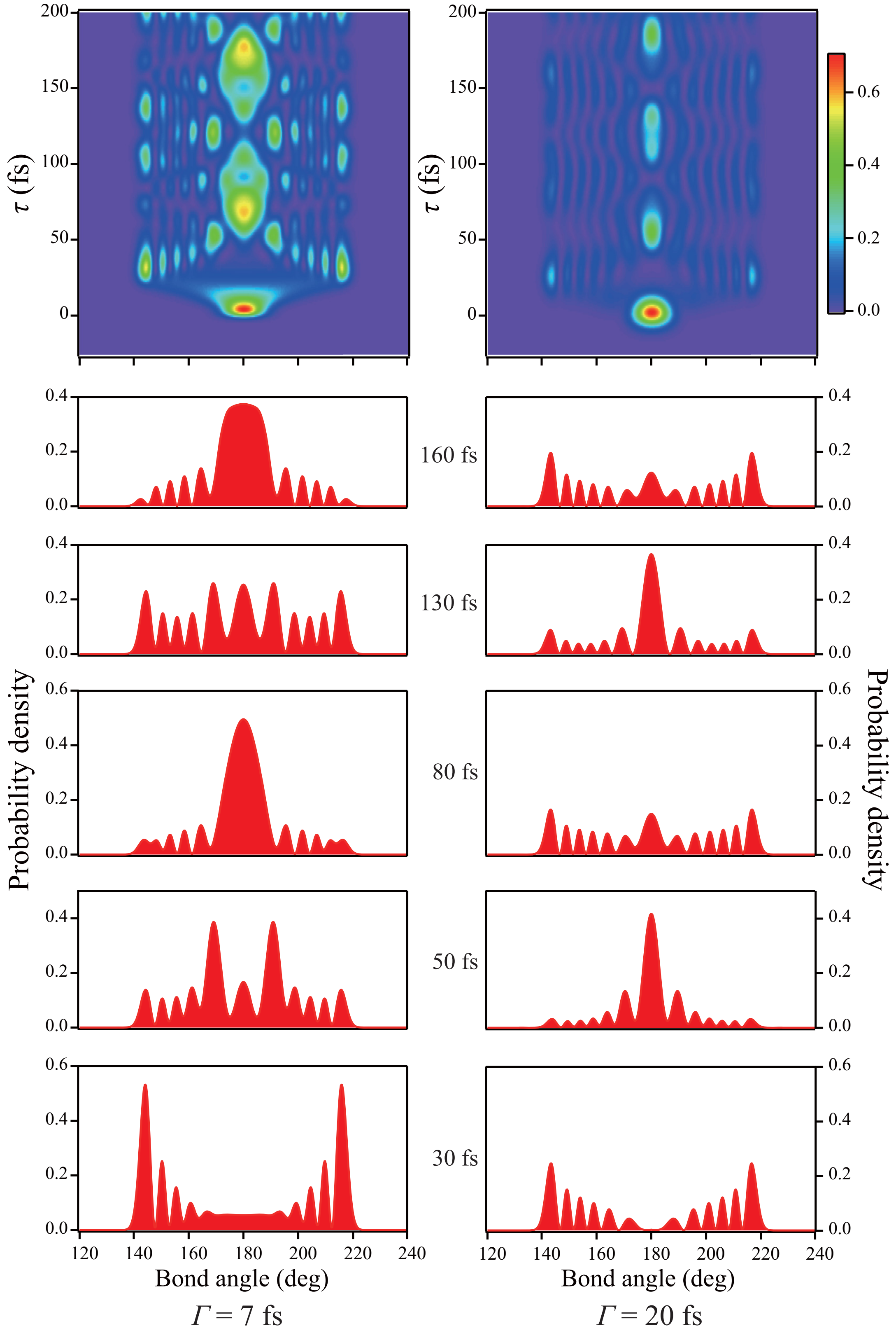

FIG. 8. Nuclear wave-packet evolutions on the state ${}^1B_2$ state of the CS_2 molecule. Left column: laser intensity of $I_0 = 3.0\times10^{11}$ W/cm^2 with pulse width of $\Gamma = 7$ fs. Right column: laser intensity of $I_0 = 3.0\times10^{11}$ W/cm^2 with pulse width of $\Gamma = 20$ fs. Upper panels: the wave-packet evolutions expressed as functions of the delay time τ and S–C–S bond angle. Lower panels: cross sections at $\tau = 30$, 50, 80, 130, and 160 fs of the upper panels. Vertical scales of $|\chi_e(\boldsymbol{R},t)|^2$ are normalized intensities; the norm of $\chi_g(\boldsymbol{R})$ is normalized to unity, so that the integral of $|\chi_e(\boldsymbol{R},t)|^2$ over the bending nuclear coordinate $\boldsymbol{R}$ yields the population of the electronic excited state; 24.4% for $I_0 = 3.0\times10^{11}$ W/cm^2 and $\Gamma = 7$ fs, and 12.7% for $I_0 = 3.0\times10^{11}$ W/cm^2 and $\Gamma = 20$ fs.

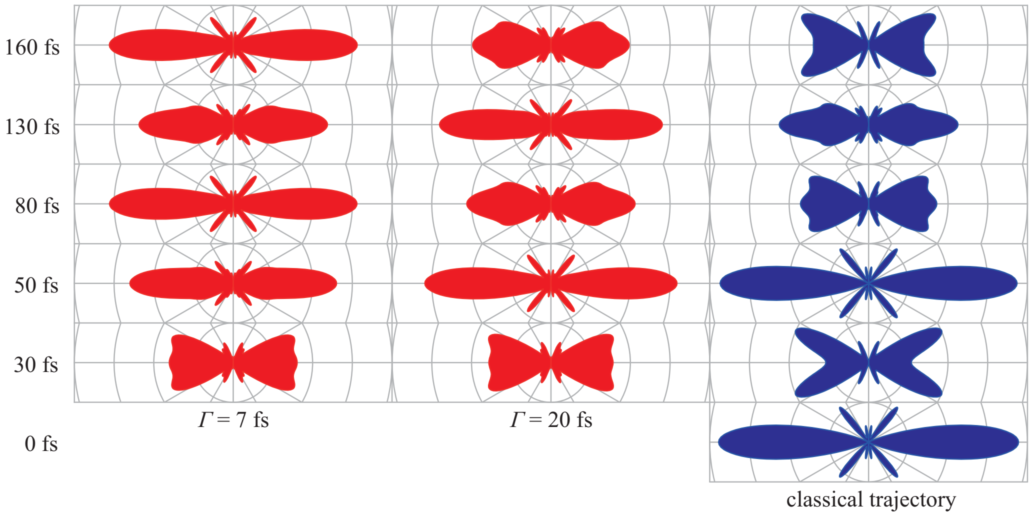

FIG. 9. Time-resolved C 1s XPD profiles of CS$_2$ molecules. The delay times are written on the left of the panel. Left: laser intensity of $I_0 = 3.0\times10^{11}$ W/cm^2 with pulse width of $\Gamma = 7$ fs, middle: laser intensity of $I_0 = 3.0\times10^{11}$ W/cm^2 with pulse width of $\Gamma = 20$ fs, and right: a classical trajectory.

130 fs. The period of the oscillation is about 80 fs. This is consistent with the experimental results of time-resolved photoelectron imaging by Horio and co-workers [40,41], who prepared the wave packets by means of a pump laser with $\Gamma = 7$ fs and $I_0 = 3.0\times10^{11}$ W/cm^2. However, it should be emphasized that the oscillation phases of the nuclear wave packets for $\Gamma = 7$ and 20 fs are different from each other.

We simulated the time-resolved C 1s XPD profiles of CS$_2$ molecules probed by ultrafast XFEL pulses as a function of pump–probe delay time τ, using the vibrational wave-packet evolution on the $^1B_2\,(^1\Sigma_u{}^+)$ state and the XPD profiles $d\sigma/d\hat{\boldsymbol{k}}(\boldsymbol{R})$. In the calculations of the XPD profiles at a fixed bond angle, we selected an XFEL photon energy of 413 eV, which is 120 eV above the C 1s ionization threshold of 293 eV [42]. Figure 9 shows the simulation results of the time-resolved C 1s XPD profiles. The areas surrounding the XPD profiles are normalized to unity. In the classical trajectories calculations, we prepared the excited states through the sudden approximation. In this approximation the relevant trajectories are irrelevant to the pulse width.

The time-resolved XPD profiles for $\Gamma = 7$ and 20 fs and the classical trajectories exhibit striking differences in terms of both their oscillation phases and shapes, reflecting the remarkable differences of the nuclear wave-packet evolutions for $\Gamma = 7$ and 20 fs. In contrast to the vibrational wave packets of the I$_2$ molecules, the bending vibrational wave packets of the CS$_2$ molecules change the molecular symmetry from $D_{\infty h}$ to C_{2v}. This necessarily causes a considerable change in the overall molecular structure of the CS$_2$ molecules. Consequently, the time-dependent XPD profiles $d\sigma/d\hat{\boldsymbol{k}}(\boldsymbol{R},\tau)$ of the CS$_2$ molecules are highly sensitive to change in the molecular structure, as can be observed from Figs. 8 and 9. This is because the time-dependent XPD profiles $d\sigma/d\hat{\boldsymbol{k}}(\boldsymbol{R},\tau)$ reflect the transient molecular structure at delay time τ, which dramatically varies during the molecular symmetry change from $D_{\infty h}$ to C_{2v}.

IV. SUMMARY

Based on both the nuclear wave-packet and MS-XPD calculations, we performed the simulations of the time-dependent XPD profiles, which can be measured by the pump–probe experimental scheme. Our results raise the following points of interest. The time-dependent I$_2$ I 3s XPD profiles obtained using the nuclear wave-packet evolution are similar to those predicted by the classical trajectory for nuclear motions, although the fine structures in the latter are blurred in the former by the spread of the nuclear wave packet. For CS$_2$ molecules, the bending vibrational wave packets depending on the temporal pulse widths of the pump lasers exhibit complicated shapes, and their oscillation period differs from that for the classical trajectory. Accordingly, the time-dependent C 1s XPD profiles based on the wave-packet calculations strikingly differ from those of the classical motions.

Very recently, direct measurements of vibrational wave packets of the I$_2$ molecules have been reported by means of ultrafast electron diffraction [43] and x-ray diffraction [44]. The former has demonstrated high sensitivity to not only the position but also to the shape of the periodic vibrational wave packets. The latter has succeeded in visualizing dispersion, dissociation, and rotational dephasing of the wave packets. These successful results encourage researchers who are developing the ultrafast XPD in gas-phase molecules in their imaging studies because photoionization cross sections are considerably larger than the cross sections of x-ray scattering and high-energy electron scattering.

ACKNOWLEDGMENTS

We thank Dr. Kaori Niki, Dr. Shin-ichiro Minemoto, Dr. Takehisa Konishi, and Professor Hirohumi Sakai for fruitful discussions. This work was supported by JSPS KAKENHI Grants No. 16J01519 and No. 16H02132.

[1] T. Elsaesser and M. Woerner, J. Chem. Phys. **140**, 020901 (2014).

[2] J. Xu, C. I. Blaga, P. Agostini, and L. F. DiMauro, J. Phys. B **49**, 112001 (2016).

[3] G. H. Stout and L. H. Jensen, *X-ray Structure Determination: A Practical Guide*, 2nd ed. (Wiley, Hoboken, New Jersey, USA, 1989).

[4] G. Rhodes, *Crystallography Made Crystal Clear*, 3rd ed. (Academic Press, San Diego, 2006).

[5] H. M. Berman *et al.*, Acta Crystallogr., Sect. D: Struct. Biol. **58**, 899 (2002).

[6] *Stereochemical Applications of Gas-Phase Electron Diffraction, Part A and B*, edited by I. Hargittai and M. Hargittai (Wiley-VCH, Hoboken, New Jersey, USA, 1996).

[7] P. Emma *et al.*, Nat. Photon. **4**, 641 (2010).

[8] T. Ishikawa *et al.*, Nat. Photon. **6**, 540 (2012).

[9] A. H. Zewail, Annu. Rev. Phys. Chem. **57**, 65 (2006).

[10] J. Küpper *et al.*, Phys. Rev. Lett. **112**, 083002 (2014).

[11] M. P. Minitti *et al.*, Phys. Rev. Lett. **114**, 255501 (2015).

[12] J. M. Budarz, M. P. Minitti, D. V. Cofer-Shabica, B. Stankus, A. Kirrander, J. B. Hastings, and P. M. Weber, J. Phys. B **49**, 034001 (2016).

[13] F. Krasniqi, B. Najjari, L. Strüder, D. Rolles, A. Voitkiv, and J. Ullrich, Phys. Rev. A **81**, 033411 (2010).

[14] M. Kazama, T. Fujikawa, N. Kishimoto, T. Mizuno, J. Adachi, and A. Yagishita, Phys. Rev. A **87**, 063417 (2013).

[15] X. Wang, A.-T. Le, C. Yu, R. R. Lucchese, and C. D. Lin, Sci. Rep. **6**, 23655 (2016).

[16] N.-T. Nguyen, R. R. Lucchese, C. D. Lin, and A.-T. Le, Phys. Rev. A **93**, 063419 (2016).

[17] R. Boll *et al.*, Phys. Rev. A **88**, 061402(R) (2013).

[18] D. Rolles *et al.*, J. Phys. B **47**, 124035 (2014).

[19] R. Boll *et al.*, Faraday Discuss. **171**, 57 (2014).

[20] K. Nakajima *et al.*, Sci. Rep. **5**, 14065 (2015).

[21] A. Yagishita, J. Electron Spectrosc. Relat. Phenom. **200**, 247 (2015).

[22] S. Minemoto *et al.*, Sci. Rep. **6**, 38654 (2016).

[23] I. Maruyama, T. Sako, and K. Yamanouchi, J. Phys. B **37**, 3919 (2004).

[24] K. Takahashi and K. Ikeda, J. Chem. Phys. **99**, 8680 (1993).

[25] T. Fujikawa, J. Phys. Soc. Jpn. **50**, 1321 (1981).

[26] H. Shinotsuka, H. Arai, and T. Fujikawa, Phys. Rev. B **77**, 085404 (2008).

[27] M. Kazama, H. Shinotsuka, T. Fujikawa, M. Stener, P. Decleva, J. Adachi, T. Mizuno, and A. Yagishita, J. Electron Spectrosc. Relat. Phenom. **185**, 535 (2012).

[28] R. D. Cowan's Atomic Structure Code, http://www.tcd.ie/Physics/people/Cormac.McGuinness/Cowan/

[29] D. M. Chase, Phys. Rev. **104**, 838 (1956).

[30] J. R. Wiesenfeld and R. H. Young, Chem. Phys. **58**, 51 (1981).

[31] K. P. Huber and G. Herzberg, *Molecular Spectra and Molecular Structure*, Constants of Diatomic Molecules Vol. IV (Van Nostrand-Reinhold, New York, 1979).

[32] F. Martin, R. Bacis, S. Churassy, and J. Vergès, J. Mol. Spectrosc. **116**, 71 (1986).

[33] J. Tellinghuisen, J. Chem. Phys. **134**, 084301 (2011).

[34] C. Cohen-Tannoudji, J. Dupont-Roc, and G. Grynberg, in *Atom-Photon Interactions: Basic Processes and Applications* (Wiley-VCH, Hoboken, New Jersey, USA, 1998), pp. 203–204.

[35] *Photoemission in Solids I: General Principles*, edited by M. Cardona and L. Ley (Springer-Verlag, Berlin, 1978).

[36] A. E. Douglas and I. Zanon, Can. J. Phys. **42**, 627 (1964).

[37] R. J. Hemley, D. G. Leopold, J. L. Roebber, and V. Vaida, J. Chem. Phys. **79**, 5219 (1983).

[38] M. F. Arendt and L. J. Butler, J. Chem. Phys. **109**, 7835 (1998).

[39] K. Sunanda, A. Shastri, A. K. Das, and B. N. Raja Sekhar, J. Quantum Spectrosc. Radiat. Transfer **151**, 76 (2015).

[40] T. Horio, R. Spesyvtsev, and T. Suzuki, Opt. Express **21**, 22423 (2013).

[41] R. Spesyvtsev, T. Horio, Y.-I. Suzuki, and T. Suzuki, J. Chem. Phys. **142**, 074308 (2015).

[42] C. J. Allan, U. Gelius, D. A. Allison, G. Johansson, H. Siegbahn, and K. Siegbahn, J. Electron Spectrosc. Relat. Phenom. **1**, 131 (1972–1973).

[43] J. Yang *et al.*, Phys. Rev. Lett. **117**, 153002 (2016).

[44] J. M. Glownia *et al.*, Phys. Rev. Lett. **117**, 153003 (2016).